Journal of Materials Chemistry A

PAPER

View Article Online
View Journal | View Issue

Cite this: J. Mater. Chem. A, 2025, 13, 37614

Nanoarchitectonics of carbon nitride/NiO/Zn_3N_2 heterointerfaces for bifunctional applications in electrocatalytic water splitting and coin cell supercapacitors

Tanuja Singh,[a] Deepak Deepak,[a] Abhishek Panghal,[a] Shailendra Kumar Saxena,[b] Barnali Mahato,[c] Abhishek S. Shekhawat[b] and Susanta Sinha Roy*[a]

The advancement of effective and durable electrocatalysts for water splitting and high-performance supercapacitors is essential for sustainable energy conversion and storage. Integrating transition metal heteroatoms can be a pivotal technique to fabricate nanostructures for such bifunctional applications. In this regard, we report graphitic carbon nitride/NiO/Zn_3N_2 heterointerfaces through a single-step pyrolysis method for the oxygen evolution reaction (OER) and coin cell supercapacitor devices. The synergetic interaction between NiO and Zn_3N_2 advances charge transfer kinetics and augments the electronic structure, while g-C_3N_4 provides a conductive network and additional active sites. Optimized sample NZN400 showed exceptional OER performance with a low overpotential value of 350 mV at 50 mA cm^{-2}, besides a low Tafel slope and high turnover frequency value. In addition, NZN400 electrodes showed a high specific capacitance value of 124 mF cm^{-2} at 2 mA cm^{-2} for the half-cell and 19.92 mF cm^{-2} at 0.2 mA cm^{-2} for the coin cell device. The fabricated device exhibited excellent cycling stability over 10 000 GCD cycles with a capacitance retention of 95.7% and coulombic efficiency of 99.4% at 0.4 mA cm^{-2} and was able to power up several commercial LEDs, a digital hygrometer, and a digital stopwatch for prolonged durations. The results highlight an effective approach for integrating transition metal oxide/nitride-based compounds with carbon-based materials, aimed at developing economical and high-performance nanostructured materials for electrochemical energy applications.

Received 23rd July 2025
Accepted 28th September 2025

DOI: 10.1039/d5ta05959c

rsc.li/materials-a

1. Introduction

Electrochemical energy conversion and storage technologies play a pivotal role in the transition toward sustainable energy systems, addressing the global demand for clean and efficient power sources. Among these technologies, water electrolysis and energy storage systems, such as supercapacitors, have gained significant attention due to their potential to drive sustainable energy solutions.[1,2] Water electrolysis enables green hydrogen production by splitting water into hydrogen and oxygen using renewable electricity, serving as a key pathway for clean fuel generation.[3] Meanwhile, supercapacitors offer high-power energy storage with rapid charge–discharge capabilities, making them ideal for applications requiring burst energy delivery.[4] Typical water splitting comprises two half-cell reactions: the hydrogen evolution reaction (HER) at the cathode and the oxygen evolution reaction (OER) at the anode. While both reactions are integral to overall efficiency, the OER remains a primary bottleneck due to its inherently sluggish kinetics, attributed to the involvement of multiple proton-coupled electron transfer steps.[5] Traditionally, noble metal-based catalysts such as platinum (Pt), iridium (Ir), and ruthenium (Ru) have been employed for electrocatalysis; however, their exorbitant cost and limited terrestrial abundance severely restrict large-scale implementation.[6,7] Consequently, the development of highly efficient, earth-abundant, and cost-effective electrocatalysts for the OER is imperative to enhance the overall efficiency of water splitting and render hydrogen production economically viable. Recent research efforts have focused on transition metal-based materials, heterointerfaces, and engineered nanostructures to augment catalytic activity, stability, and electronic conductivity. In this context, the exploration of novel material architectures and advanced synthesis strategies for OER catalysts is pivotal in advancing water-splitting technologies toward scalable and practical applications.[8–10]

On the other hand, in the realm of energy storage, supercapacitors have emerged as vital electrochemical devices due to

[a]Department of Physics, School of Natural Sciences, Shiv Nadar Institution of Eminence, Gautam Budh Nagar 201314, Uttar Pradesh, India. E-mail: susanta.roy@snu.edu.in

[b]Department of Physics and Nanotechnology, College of Engineering and Technology, SRM Institute of Science and Technology, Kattankulathur, Chennai, India

[c]Instrumentation and Applied Physics Department, Indian Institute of Science, Bangalore 560012, India

their rapid charge–discharge capability, high power density, and exceptional long-term stability.[11] However, electrodes composed of a different material often exhibit high energy density, but they are lacking in terms of long-term stability, and fast charge–discharge rates, thereby restricting overall performance.[12] To address this limitation, symmetric supercapacitors (SCs), which utilize the same electrode materials for the anode and cathode, have been extensively investigated. SCs offer a simplified fabrication and, due to the balanced charge storage mechanism, they exhibit higher stability and longer lifespan, making them a promising alternative for next-generation energy storage systems.[13] Coin-cell symmetric supercapacitors, which are essential for assessing the electrochemical performance of electrode materials in a consistent and reproducible way, are an example of such systems.[13]The compact and robust design ensures accurate electrode spacing, optimal electrolyte distribution, and a tightly sealed compressed environment, thereby reducing external variables that may influence performance.[14]

The advancement of electrode materials is essential for improving energy storage and conversion performance, demanding high electrochemical activity, large surface area, superior areal-specific capacitance, and structural durability.[15,16] Developing novel materials with tailored properties is crucial for optimizing efficiency and enabling practical energy storage applications. Nonetheless, the domain of material engineering in pursuit of a bifunctional nature in electrochemical energy conversion and storage continues to be underdeveloped.

Transition metal oxides, nitrides, and sulphides have attracted substantial attention for energy storage and conversion applications in recent years because of their structural tunability, high performance, and abundance.[17–19] The incorporation of dual-metal systems improves catalytic performance by facilitating rapid charge transfer and leveraging synergistic effects, among other strategies, to enhance the properties of these materials. Nickel oxide (NiO) is a transition metal oxide that is extensively investigated due to its exceptional electrochemical properties.[20] In a recent study, Deling Wang *et al.*[21] published a CoN/Ni/NiO composite that exhibited impressive OER activity with an overpotential of 114 mV at 10 mA cm^{-2}. In NiO, the Ni^{2+}/Ni^{3+} redox couple is present, which facilitates rapid and reversible charge transfer, thereby improving the charge storage capability. Additionally, it demonstrates a high experimental and theoretical capacitance.[22] The intrinsic stability of NiO guarantees long-term electrochemical performance, while its conductivity is substantially enhanced by nano-structuring.[23] Furthermore, NiO functions as an effective catalyst for the oxygen evolution reaction (OER) in alkaline environments.[24] NiO is frequently combined with metal nitrides, sulphides, or carbon-based materials to further improve its electrochemical kinetics and conductivity. Derived from earth-abundant precursors like urea and melamine, graphitic carbon nitride (g-C_3N_4) is one of the most promising carbon-based materials for energy applications.[25] In a study conducted by Kousik Bhunia *et al.*[26] the NiO NPs/g-C_3N_4 electrocatalyst exhibited an optimistic OER performance by achieving an overpotential of 360 mV at 10 mA cm^{-2} current density. Highly effective for both the hydrogen evolution reaction (HER) and the oxygen evolution reaction (OER), g-C_3N_4 is a metal-free electrocatalyst and support material with nitrogen-rich functional groups (–NH_2 and –C═N) that provide plentiful active sites for redox processes. Nevertheless, the intrinsic conductivity of pure g-C_3N_4 is restricted; hence, metal doping (*e.g.*, Ni, Co, and Zn) or coupling with conductive materials such as graphene and carbon nanotubes (CNTs) would help to improve electron transport properties.[27,28] Often mixed with transition metal oxides, sulphides, or nitrides to improve charge storage performance, graphitic carbon nitride (g-C_3N_4) is a potential material for hybrid supercapacitors and water-splitting applications.[29] Among several metal nitrides, Zn_3N_2 is among the least investigated despite its superior charge concentration, high electron conductivity, nitrogen-rich framework, outstanding stability in both alkaline and neutral environments, and cost-effectiveness.[30] The manufacturing of a CoN/Zn_3N_2 composite for asymmetric supercapacitors (ASCs) leads to a specific capacitance of 75.4 F g^{-1}, therefore highlighting its potential for advanced energy storage uses in a report by Ravikant Adalati *et al.*[31]

Huifang Yang[32] reported a carbon nitride/NiO/CoN-based composite and showed its possible electrochemical uses. However, low stability and high cost of CoN limited the scalability and the practical applications. Inspired by this, herein, we report synthesis of a g-C_3N_4/NiO/Zn_3N_2 nanostructure using the one step pyrolysis method for the electrochemical oxygen evolution reaction and high-performance coin cell supercapacitors. In contrast to the above reported work, Zn_3N_2, which has a narrower bandgap than Co-based nitrides, facilitates increased charge transfer and electron mobility. While retaining outstanding electrochemical characteristics, this method provides a more cost-effective, durable, and high-performance alternative. Optimized nanostructure NZN400 showed a low overpotential value of 350 mV at 50 mA cm^{-2} and minimal Tafel slopes (85 mV per decade) for the oxygen evolution reaction in alkaline media. Additionally, NZN400 exhibited a high specific capacitance value of 124 mF cm^{-2} at 2 mA cm^{-2} for the half-cell and 19.92 mA cm^{-2} at 0.2 mA cm^{-2} for the coin cell symmetric supercapacitor device with a capacitance retention of 95.7% sustained after 10 000 GCD cycles, effectively powering a digital hygrometer, a stopwatch, and commercial LEDs for an extended duration.

2. Experimental section

2.1 Chemicals

All compounds used in this study were of analytical grade and used without additional purification. Zinc nitride hexahydrate, urea, and potassium hydroxide (KOH, 99%) were acquired from Sigma-Aldrich, whilst nickel foam (1.5 mm thickness) was sourced from Global Nanotech.

2.2 Materials synthesis

2.2.1 Fabrication of g-C_3N_4/NiO/Zn_3N_2 electrodes. 2 g of urea and 0.5 g of zinc nitrate hexahydrate were dissolved in

10 mL of deionized water for electrode fabrication as shown in Fig. 1a(i). Then nickel foam was submerged in the solution overnight. While $Zn(NO_3)_2 \cdot 6H_2O$ and Ni provided dual transition metal ions to enable fast redox reactions, urea was introduced to create surface defects and a nano-scaled porous morphology. To maximize their structural and electrochemical characteristics, the prepared electrodes were next air-annealed for 2 hours at 200 °C, 400 °C, and 600 °C. The samples were labelled as NZN200, NZN400, and NZN600, respectively. NiO/g-C_3N_4 that was annealed at 400 °C was prepared using urea and Ni foam and labelled as NU400. Similarly, NZ400 was prepared using zinc nitrate hexahydrate and Ni foam. Fig. S12 shows the original image of grown nanostructures.

2.2.2 Fabrication of coin cell supercapacitor devices. NZN400 coin-cell supercapacitor devices were assembled in a standard CR2032 configuration. Whatman® cellulose filter paper pre-soaked in an aqueous Na_2SO_4 electrolyte was sandwiched between two identical NZN400 square electrodes (0.5 cm × 0.5 cm). The configuration of the NZN400 coin cell supercapacitor is shown in Fig. 1a(ii)

2.3 Characterization details

XRD of fabricated electrodes was carried out in couple theta-two theta diffraction (Bruker D8 Discover) using Cu–K alpha radiation. Raman spectroscopy was conducted using a micro-Raman

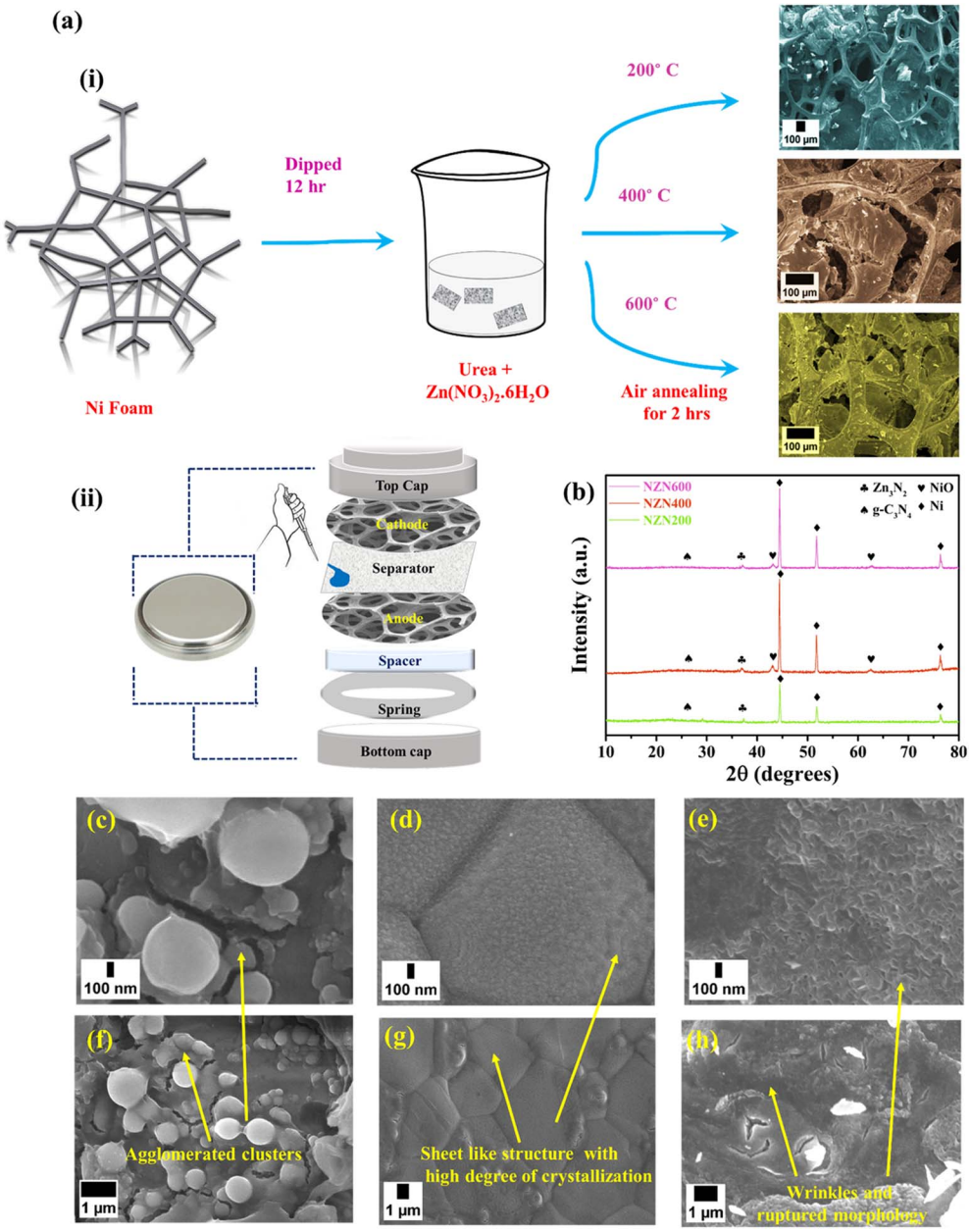

Fig. 1 (a) (i) Schematic of the synthesis process of graphitic nitride/NiO/Zn_3N_2 heterointerfaces, (ii) schematic of fabrication of a coin cell device, (b) XRD patterns of NZN200, NZN400 and NZN600, (c) & (f) FESEM image of NZN200, (d) & (g) FESEM images of NZN400 and (e) & (h) FESEM images of NZN600.

spectrometer (STR) with a 532 nm argon-ion laser source, 2.5 mW power output, and a 20× objective lens. Surface morphology was studied using a FESEM JEOL JSM PLUS. X-ray photoelectron spectroscopy (XPS) was conducted using a Kratos Analytical Axis Supra instrument equipped with a monochromatic Al Kα (1486.7 eV) X-ray excitation source.

2.3.1 Electrochemical measurement details. An Autolab Potentiostat/Galvanostat 302N (Metrohm B.V., Utrecht, Netherlands) running Nova software (version 1.10) was used for all electrochemical experiments. Techniques such as Linear Sweep Voltammetry (LSV), Electrochemical Impedance Spectroscopy (EIS), and Cyclic Voltammetry (CV) were used for evaluation of electrochemical performance. Measurements were made using a three-electrode setup. Ag/AgCl served as the reference electrode, the $NiO/Zn_3N_2/g\text{-}C_3N_4$ composite served as the working electrode and platinum (Pt) served as the counter electrode. Using LSV and a scan rate of 20 mV s^{-1}, the Oxygen Evolution Reaction (OER) polarisation curves were obtained a potential range of 0 to 1 V. CV was used to compute the double-layer capacitance (C_{dl}) between 0.1 and 0.3 V at scan rates of 20, 40, 60, 80, and 100 mV s^{-1}. The following equation was used to derive the RHE scale from observed potentials:

$$E_{RHE} = E_{Ag/AgCl} + 0.059\ pH + 0.197$$

The long-term stability was assessed by a 22 h chronopotentiometry test at a current of 10 mA. All the electrochemical measurements were conducted at room temperature.

3. Results and discussion

3.1 X-ray diffraction (XRD) analysis

The XRD technique provides a hint towards crystallographic orientations and structural composition of synthesized nanostructures.[33] Fig. 1b shows a comparative XRD spectrum of $NiO/Zn_3N_2/g\text{-}C_3N_4$ heterointerfaces fabricated at various annealing temperatures. The diffraction peaks observed at 43.3° and 62.4° can be assigned to the (200) and (220) planes of cubic NiO present in NZN200, NZN400, and NZN600.[34] These peaks become more noticeable as the annealing temperature increases from 200 °C to 400 °C, therefore suggesting increased crystallinity. Furthermore, peaks at 44.5°, 52.1° and 76.3° correspond to the (111), (200), and (220) planes of metallic Ni due to nickel foam.[34] A slight hump at (~26°) is attributed to $g\text{-}C_3N_4$.[35] To further validate this, Fig. S1(b) presents the XRD spectrum of NZ400 (NiO/Zn_3N_2), illustrating the absence of this peak. The peak at 37.3° corresponds to the (400) plane owing to Zn_3N_2.[36] However, at higher temperatures, the intensity of these peaks lowers due to lower nitrogen concentration (Fig. S1(b)). All JCPDS files with NZN heterostructures are shown in Fig. S26.

3.2 Morphological characterization

3.2.1 FESEM analysis. Fig. 1c–h shows the morphology of the synthesized heterointerfaces. NZN200 exhibits a spherical nanoparticle-like morphology with a certain degree of agglomeration. This nano-scaled morphology of NZN200 indicates particle sizes ranging from 100 nm to 1.25 μm (Fig. 1c). Fig. 1f shows distant nanoparticles forming clusters, which implies that the surface has a high porosity and incomplete growth. The structure appears to have a porous interconnected network with significant voids at 100 nm, which enhances the pathways for electron transport and electrolyte penetration. A well-defined polygonal or sheet-like morphology arises for NZN400, suggesting enhanced grain growth. Fig. 1d illustrates the growth of grain formations throughout the samples, which suggests a well-defined morphology. The interconnected network is preserved, but the material appears denser and more robust, assuring improved mechanical stability while maintaining suitable porosity for efficient mass transfer (Fig. 1g). The evaporation of volatile components in NZN600 results in a highly porous and wrinkled morphology as shown in Fig. 1e. The structure exhibits disordered nanopores with an irregular, fragmented morphology at the micrometre scale (Fig. 1h). Fig. S2 illustrates the FESEM image of NZN400 at varying scales following the electrochemical experiments conducted, in addition to the EDS spectrum. Therefore, electrocatalysis and charge storage applications can be improved through the optimization of porosity, structural stability, and well-defined grains.

3.2.2 TEM analysis. The TEM, HRTEM, and SAED patterns for the NZN200, NZN400, and NZN600 samples are illustrated in Fig. 2. Using TEM, we can achieve a more comprehensive understanding of the formation of morphology at different temperatures. The TEM image (NZN200) at 100 nm in Fig. 2a clearly demonstrates the layered sheet-like structure with narrow, wrinkled nanosheets, indicating the presence of $g\text{-}C_3N_4$. The structure appears to be loosely packed, suggesting an improper degree of grain formation for NZN200. The inset shows the corresponding SAED patterns for NZN200, which is composed of diffuse, indistinct rings that are likely the result of incomplete phase formation at this lower temperature. In Fig. 2d, the HRTEM image of NZN200 confirms the presence of $g\text{-}C_3N_4$, having a *d*-spacing of 0.331 nm, Zn_3N_2, corresponding to a *d*-spacing of 0.171 nm, and NiO, with (111) corresponding to 0.248 nm.[36–38] Fig. 2b shows the TEM image of NZN400 with well-defined nanosheets, possessing superior structural integrity. The composite's increased compactness implies that it has undergone adequate phase formation. The inset shows a corresponding SAED pattern showing distinct diffraction patterns. Fig. 2e shows the HRTEM image of NZN400 showing the relative *d*-spacing of the nanostructure. The morphology of NZN600 reveals aggregated irregularly shaped nanoparticles, which suggests excessive grain growth (Fig. 2c). The structure is devoid of the sheet-like characteristics observed in NZN200 and NZN400, which implies that $g\text{-}C_3N_4$ is destroyed at this elevated temperature. The inset shows the respective SAED patterns. Fig. 2f shows the *d* spacing of the respective nanostructure. Further TEM elemental mapping (Fig. 2g) confirms the uniform distribution of all elements, *i.e.*, Ni, Zn, N, O, and C. The presence of these elements signifies the successful formation of $NiO/ZN_3N_2/g\text{-}C_3N_4$. Homogeneous dispersion of the elements supports and improves the catalytic activity. Fig. S3a and b show the elemental mapping analysis of NZN200 and NZN600, depicting all elements present.

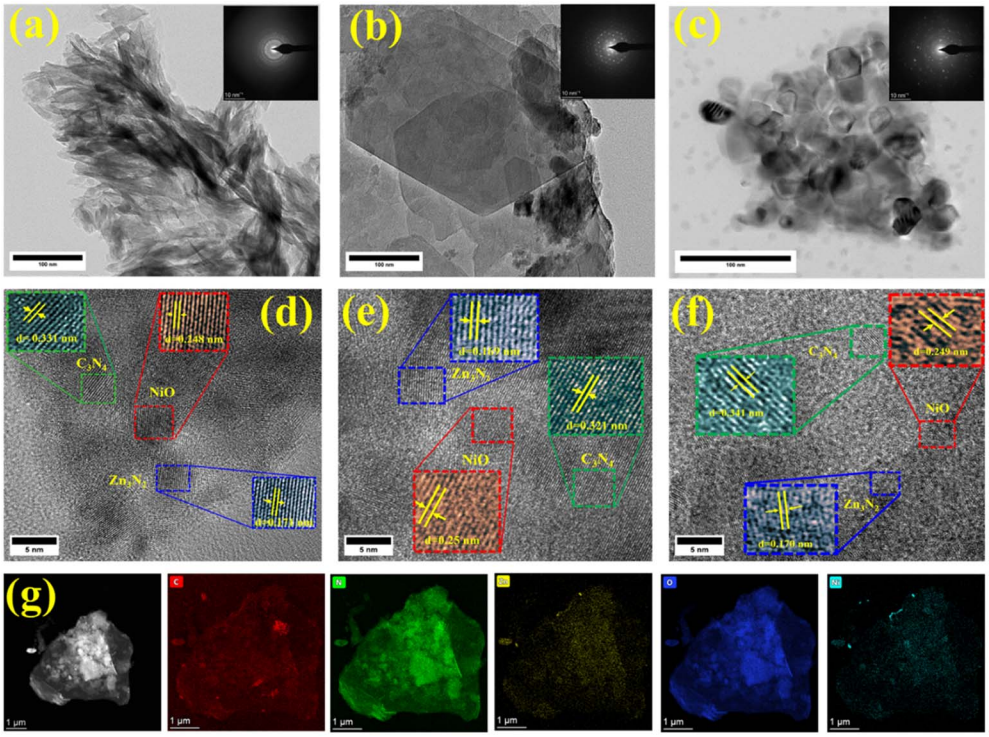

Fig. 2 (a)–(c) TEM image of NZN200, NZN400, and NZN600, respectively. (d)–(f) HRTEM images of NZN200, NZN400 and NZN600 respectively; (g) elemental mapping of NZN400.

3.3 Compositional analysis

The XPS spectra offer critical insights into the elemental composition, oxidation states, and chemical interactions of NiO/g-C_3N_4/Zn_3N_2 composites subjected to annealing at different temperatures. Fig. 3(a)–(e) represents the deconvoluted XPS spectra of Ni 2p, Zn 2p, C 1s, O 1s, and N 1s, respectively. The Ni 2p spectra (Fig. 3a) of all nanostructures exhibit two primary peaks at ~855.97 eV and ~873.72 eV, which correspond to Ni $2p_{3/2}$ and Ni $2p_{1/2}$, respectively, and indicate different oxidation states of NiO.[39] Also, peaks at 854.12 eV and 872.18 eV correspond to the Ni^{2+} oxidation state, and peaks at 856.01 eV and 874.21 eV align with Ni^{3+} due to surface defects or phase formation of Ni_2O_3.[40] Two additional satellite peaks are observed at 860.93 eV and 879.56 eV. Two prominent peaks in the Zn 2p spectra (Fig. 3b) at 1022.15 eV (Zn $2p_{3/2}$) and 1044.6 eV (Zn $2p_{1/2}$) point to Zn^{2+} in Zn_3N_2.[41] The intensity of these peaks is higher in NZN400 than in NZN200, which implies that the optimal temperature is conducive to the enhanced incorporation of Zn_3N_2. NZN600 showed a slight peak broadening, which might be due to surface oxidation or nitrogen loss at higher temperatures. The C 1s spectra (Fig. 3c) illustrate peaks at 284.8 eV, 286.2 eV, and 288.5 eV attributed to C=C/C–N, C–O–C, and N–C=N, respectively.[42–44] In lower temperature ranges, *i.e.*, for NZN200 and NZN400, the presence of N–C=N indicates that graphitic carbon nitride is well preserved; however, decreased intensity in NZN600 signifies that it might have been deployed at high temperature. The O 1s spectra (Fig. 3d) of NZN200 show peaks at 531.42 eV and 532.76 eV, representing the oxidation state corresponding to Ni_2O_3 and surface adsorbed oxygen, respectively.[40] Interestingly, NZN400 and NZN6000 show a lattice oxygen peak at 529.36 eV, confirming the significant phase formation of NiO.[45] The N 1s spectra (Fig. 3e) exhibit two deconvoluted peaks at approximately 400.39 eV and 398.56 eV, which correspond to distinct nitrogen species. The pyridinic nitrogen in g-C_3N_4 is responsible for the peak at 398.56 eV.[42–44] The presence of carbon nitride is confirmed by the peak at 400.39 eV,[42–44] which is attributed to graphitic nitrogen. The intensity of the Zn–N peak decreases as the temperature increases, suggesting that nitrogen is lost at higher temperatures. The EDS analysis in Fig. S4 validates the compositional presence of NiO/g-C_3N_4/Zn_3N_2 as the temperature increases. Fig. S5 shows the elemental FESEM mapping analysis of NZN400, confirming the uniform distribution of Ni, Zn, C, O, and N. Fig. S6 shows the XPS survey spectrum of all nanostructures.

3.4 Raman spectroscopy and BET analysis

The Raman spectra of the NiO/Zn_3N_2 and graphitic carbon nitride (g-C_3N_4) hybrids show different characteristic vibrational modes. Fig. 3f shows a comparison of Raman analysis of NZN200, NZN400, and NZN600, depicting structural changes as a function of annealing temperature. A peak at about 385 cm^{-1} (in NZN200) indicates the presence of Zn_3N_2, either *via* defect-induced vibrations, intrinsic phonon modes, or probable oxygen incorporation producing a mixed phase[46] A wide band from 500–550 cm^{-1} (*i.e.* in NZN400 and NZN600) indicates to F_{2g} phonon mode and confirms the successful synthesis of nickel oxide.[47] Interestingly, Zn_3N_2 exhibits a wide band in

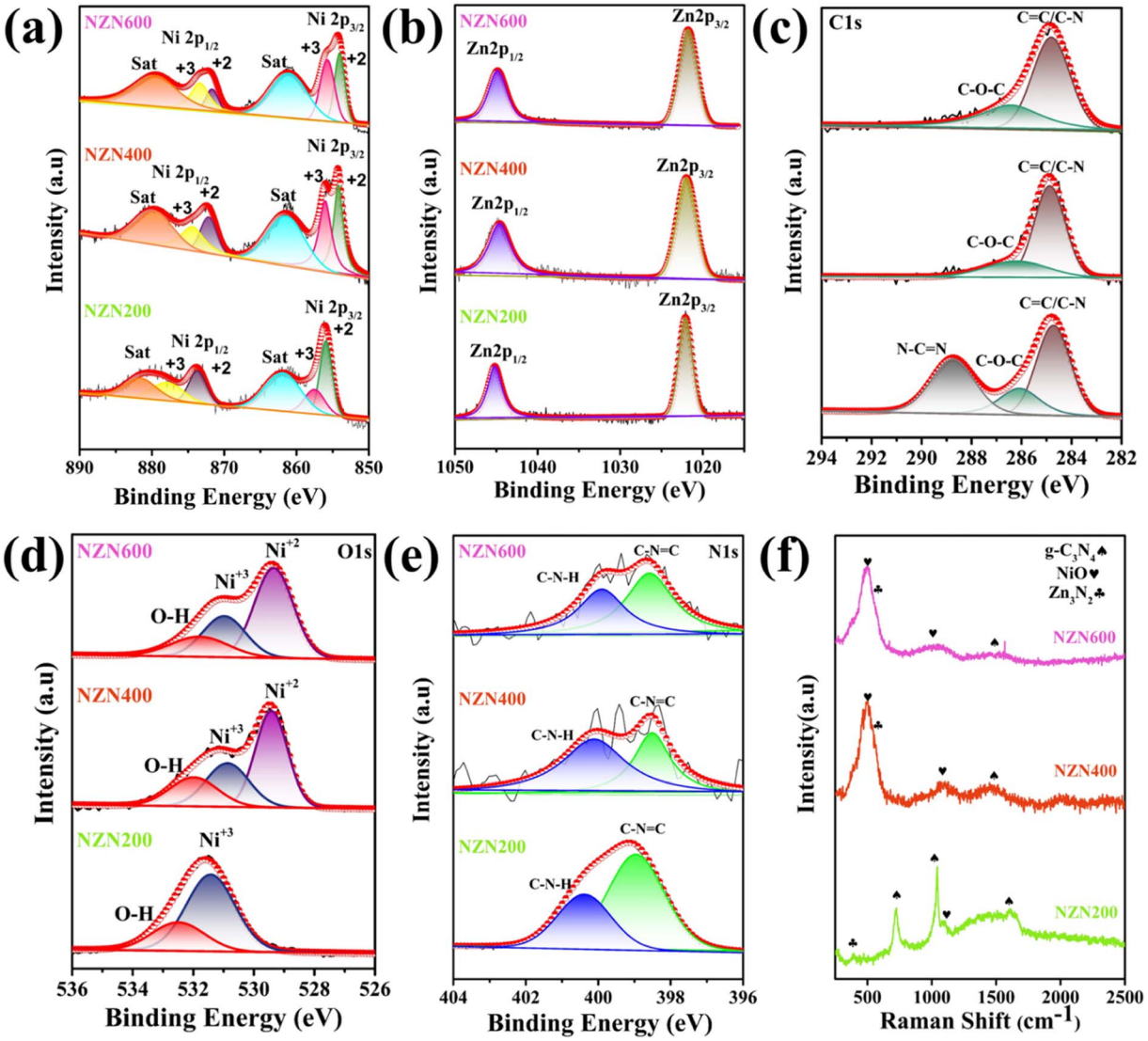

Fig. 3 Deconvoluted XPS spectra of all heterointerfaces: (a) Ni 2p, (b) Zn 2p, (c) C 1s, (d) O 1s and (e) N 1s; (f) Raman spectra of NZN200, NZN400, and NZN600.

a similar range owing to the Zn–N vibrational mode.[48] The Raman peaks within the range of 725 and 1045 cm^{-1} indicate the stretching vibrations of aromatic C–N heterocycle characteristic of graphitic carbon nitride (g-C_3N_4).[49,50] Moreover, the strong peaks seen in the 1100–1300 cm^{-1} range indicate the skeletal vibrations of C–N bonds in g-C_3N_4; the G-band of sp^2-hybridized carbon accounts for the observed peak in the 1500–1600 cm^{-1} range, further validating the presence of graphitic carbon nitride.[49,50] Fig. S1(a) displays the Raman spectra of Zn_3N_2/NiO (NZ400) and g-C_3N_4/NiO (NU400) that have been annealed at an optimized temperature of 400 °C. With samples annealed at 600 °C (NZN600), the intensity and coherence of these peaks reflect a temperature-dependent pattern whereby most Raman characteristics indicate increased crystallinity of Zn_3N_2, NiO, and g-C_3N_4. Furthermore, increased oxygen consistency because of annealing influences the carbon–nitrogen bond, which is predominantly affected by the vibrations of nickel oxide and oxynitrides. Changing the annealing temperature affects the structural evolution of the composite, thereby improving phase purity and lowering amorphous contributions found in the lower-temperature nanostructures.

3.5 BET analysis

Since the nanostructures were grown on self-supported nickel foam, we fragmented each NZN nanostructure into pieces and calculated their BET surface area (Fig. S13). NZN400 exhibited the highest surface area of 4.14 $m^2\ g^{-1}$ as compared to NZN200 and NZN600, which show the values of 3.05 $m^2\ g^{-1}$ and 1.3 $m^2\ g^{-1}$, supporting the higher electrocatalytic properties of NZN400.

3.6 Electrochemical energy conversion

To thoroughly assess the electrocatalytic properties, all the synthesized nanostructures have undergone electrochemical characterization procedures including cyclic voltammetry (CV),

linear sweep voltammetry (LSV), electrochemical impedance spectroscopy (EIS), chronopotentiometry, and symmetric testing. A three-electrode system with 1 M KOH as the electrolyte was utilized for these studies. Ag/AgCl was used as the reference electrode, platinum as the counter electrode, and NZN200, NZN400, and NZN600 as working electrodes. Important characteristics such as overpotential, Tafel slope, ECSA, R_{ct}, and R_s have been assessed to evaluate the OER performance. From a materials perspective, NiO is the main catalytic component for the OER since it supplies the main active sites for oxygen oxidation and adsorption.[51] Because of the existence of Ni^{2+}/Ni^{3+} redox couples, NiO offers a highly conductive network that improves charge transfer and fosters catalytic efficiency. Graphitic carbon nitride decreases overall resistance and facilitates charge transport *via* a conductive carbon matrix.[52] The porous nature of C_3N_4 promotes the additional active sites required for catalytic activity. To enhance catalytic activity, C_3N_4 also introduces defect sites that modify the local charge density and the oxygen binding strength. Zn_3N_2 enhances mechanical integrity and accelerates reaction kinetics by altering the electronic structure of NiO and restricting excessive adsorption. The optimal proportion of NiO, Zn_3N_2, and g-C_3N_4 in NZN400 produces synergy, leading to enhanced long-term stability, increased active site exposure, ideal oxygen adsorption energy, and efficient charge transport. Given that the OER exhibits sluggish kinetics, it is imperative to develop an electrocatalyst with enhanced performance to augment overall efficiency.[53] The charge transfer mechanism of the oxygen evolution reaction comprises four fundamental steps:

$$OH^- + N^* \rightarrow OH^N* + e^-$$

$$OH^- + OH^N* \rightarrow O^N* + H_2O + e^-$$

$$O^N* + OH^- \rightarrow OOH^N* + e^-$$

$$OOH^N* + OH^- \rightarrow N^* + O_2 + H_2O + e^-$$

where N* represents the active sites on the surface of the synthesised nanostructures.

In the NZN heterostructure, the Ni centre in NiO serves as the principal active site for the OER, the redox couples of $Ni^{2+}/Ni^{3+}/Ni^{4+}$. Upon the electrochemical sweeps in alkaline electrolyte, Ni^{2+} is first oxidized to Ni^{3+}, followed by Ni^{4+}, producing the NiOOH species, which are considered as intermediates for OER-based electrocatalysts. The anodic peaks observed in the CV curves indicate the oxidation of Ni^{2+}/Ni^{3+}. In addition, post-OER XPS analysis shows the shift in Ni 2p B.E. values towards higher B.E., further confirming oxidation of Ni^{2+}/Ni^{3+}.

Zn_3N_2 exhibits Zn–N coordination sites, which contribute effectively to the OER activity in addition to NiO. The enriched nitrogen environment provides additional adsorption sites for OH^- ions, which facilitates the formation of intermediate, *i.e.*, OH*, O*, and OOH*. Zinc does not undergo major oxidation itself under the OER activity; however, its potential in modulating the electronic structure of the heterostructure and improving the OH^- adsorption and charge redistribution is very crucial.

In addition, g-C_3N_4 has enriched nitrogen that increases the dispersion of both NiO and Zn_3N_2, further facilitating the charge transfer and stabilizing the heterostructure network. These three phases enable the close synergetic effects like increased conductivity, high ECSA, and increased exposed active sites.

Thus, the OER mechanism in our composite involves the following key steps at Ni sites:

$$Ni^{2+}–OH^- \rightarrow Ni^{3+}–OH* + e^-$$

$$Ni^{3+}–OH* \rightarrow Ni^{4+}–O* + H^+ + e^-$$

$$Ni^{4+}–O* + OH^- \rightarrow Ni^{4+}–OOH* + e^-$$

$$Ni^{4+}–OOH* \rightarrow Ni^{2+} + O_2 + OH^- + e^-$$

Zn_3N_2 modulates the electronic density at the sites of Ni through the interactions of Ni–N–Zn. In addition, it also provides Lewis basic N sites which can directly absorb the OH^- ions which further assists in the formation of OH^* and OOH^*. It also prevents the excess oxidation of NiO by stabilizing Ni^{3+}/Ni^{4+}. Overall, Zn_3N_2 introduces Zn–N moieties which can serve as the secondary adsorption sites for the OH^-. The coupling between Zn–N and Ni–O redistributes the charge density which further lowers the activation barrier for water splitting.

g-C_3N_4 participates directly through the pyridinic and graphitic N sites which interact with OH^- and serve as electron donating groups which overall accelerate the Ni^{2+}/Ni^{3+} redox conversion. The robust coupling at the heterointerface of NiO/g-C_3N_4 generates the defect rich active centres which facilitate the water splitting process.

This redox cycle is supported and accelerated by Zn–N and g-C_3N_4 sites, which assist in intermediate adsorption and charge mobility (Fig. 8a).

Since NZN400 has a higher degree of crystallization at an optimal temperature, which results in a higher proportion of nitrogen and oxygen vacancies, it is anticipated to have the best OER activity among all. The LSV polarisation curves of NZN200, NZN400, and NZN600 at a scan rate of 20 mV s^{-1} are shown in Fig. 4a. NZN400 showed the least overpotential value of 350 mV at 50 mA cm^{-2} as compared to NZN200 and NZN600, which showed 470 mV and 600 mV, respectively. NZN200 shows saturation behaviour beyond 1.6 V, which might be due to:

1. At higher overpotentials, due to deprived porosity and phase development, mass transport limitations arise, which hinder the performance.

2. In NZN200, accumulation of OER intermediates like OOH* or the evolution of gas bubbles cannot be efficiently desorbed or removed from the surface (catalyst passivation), leading to low current or saturated current response.

3. An inadequate phase leads to instability of the catalyst at high anodic potentials which further decreases the electrocatalytic activity.

Fig. S7a shows the LSV comparison profiles of pristine materials and heterointerfaces. A comparison bar graph

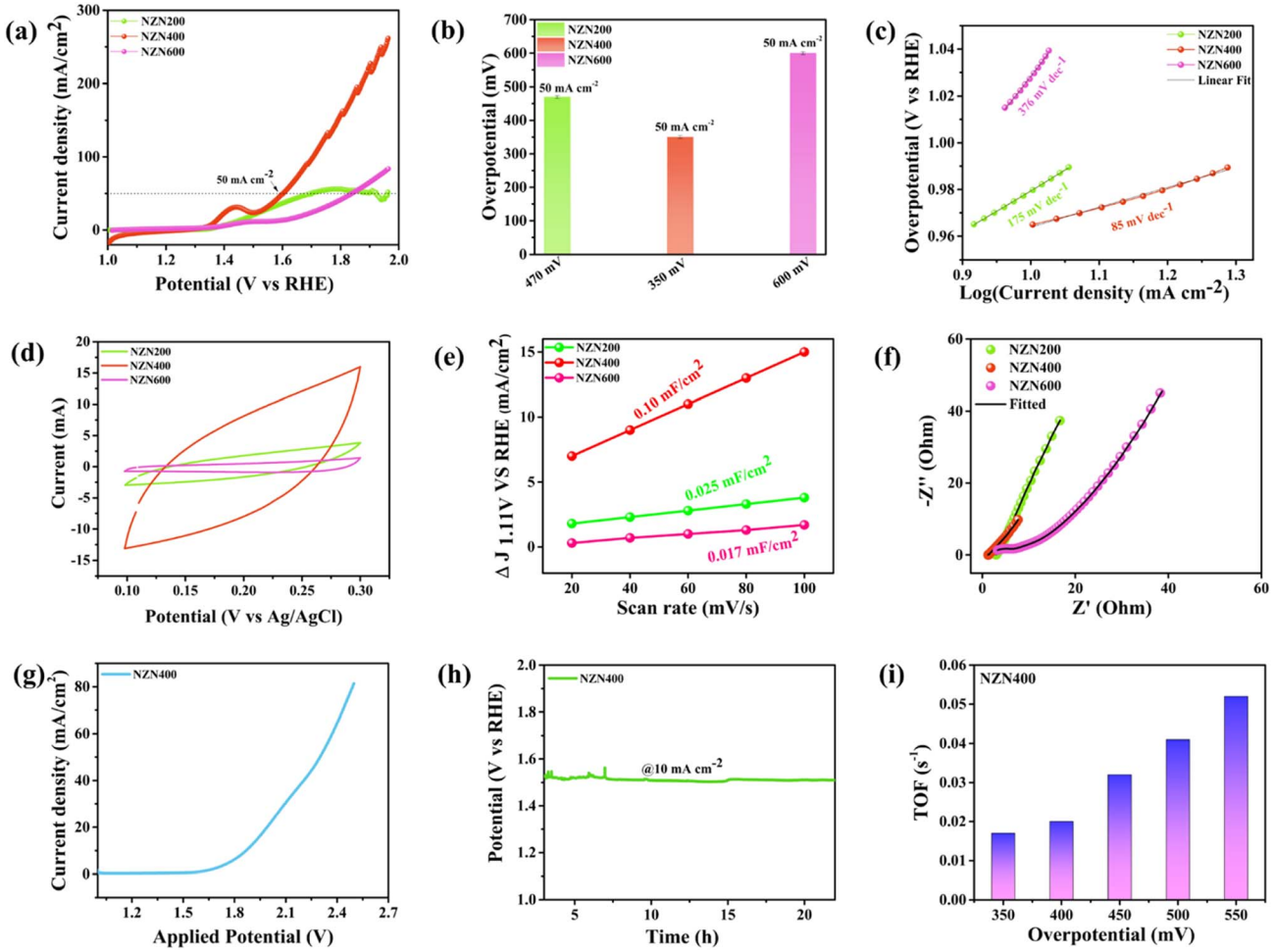

Fig. 4 (a) LSV of NZN200, NZN400 and NZN600, (b) overpotential bar graph comparison, (c) Tafel slope, (d) CV curve in non-faradaic regions, (e) C_{dl} value calculation, (f) EIS spectra of NZN200, NZN400 and NZN600, (g) full cell testing of NZN400, (h) chronopotentiometry stability test and (i) TOF *vs.* overpotential.

depicting overpotential values at 50 mA cm^{-2} is shown in Fig. 4b. The Tafel slope provides information on the kinetics of the process and reaction pathway. The reaction kinetics are better when the Tafel slope value is lower.[54] Fig. 4c shows the Tafel slope values of NZN200, NZN400, and NZN600. NZN400 shows the least Tafel slope value of 85 mV dec^{-1} as compared to NZN200 and NZN600, which showed slope values of 175 mV dec^{-1} and 376 mV dec^{-1}, respectively. This parameter demonstrates better electrocatalytic activity of NZN400 over other catalysts. Generally, a Tafel slope value close to 120 mV dec^{-1} indicates the first electron transfer step with the formation of *OH from OH$^-$ as the rate-limiting step, and a Tafel slope value of 60 mV dec^{-1} indicates the second electron transfer step with the formation of *O from *OH as the rate-determining step. A Tafel slope above 200 mV dec^{-1} reflects sluggish kinetics caused by mass transport resistance or weak intermediate adsorption.

For NZN400, the observed Tafel slope (85 mV dec^{-1}) indicates stable binding energy of OER intermediates and increased charge transfer kinetics. This behaviour can be supported by the close synergetic effects of NiO, Zn_3N_2, and g-C_3N_4 at 400 °C, which ensures the increased crystallinity, modulation of the electronic structure, and enriched redox couple sites of Ni^{2+}/Ni^{3+}. Overall, these factors combined accelerate the rate kinetics by rapid formation of intermediates and transformation of OER intermediates like OH*, O*, and OOH*. In contrast, NZN200 exhibits a higher Tafel slope value of 175 mV dec^{-1}, lacks proper phase formation, and exhibits lower conductivity due to inadequate crystallization at 200 °C. This phenomenon results in sluggish kinetics, allowing the first electron transfer step to become the rate-limiting step. NZN600 is annealed at a very high temperature and shows a Tafel slope value of 376 mV dec^{-1} and decreased electrocatalytic activity due to structural deformation or collapse of the g-C_3N_4 network and nitrogen loss from Zn_3N_2, which leads to poor intermediate stabilization and decreased active site density.

In summary, the Tafel slope variations for NZN heterostructures underline the dependence of the OER mechanism on morphology, crystallinity, and modulated electronic conductivity and available active sites.

The CV plots of NZN200, NZN400, and NZN600 at a scan rate of 100 mV s^{-1} are shown in Fig. 4d. NZN400 has a very high enclosed area that directly indicates towards a large charge

storing capacity and can be determined from the CV plots. In addition, NZN400 exhibits a higher current density than NZN200 and NZN600. Electric double layer capacitance is an additional parameter used in the analysis of catalyst activity and calculation of electrochemical active surface area (ECSA). Fig. 4e shows the C_{dl} values of all catalysts, depicting the highest value for NZN400 as compared to NZN200 and NZN600. Based on this value, ECSA for the nanostructures was calculated (SI eqn (6)) using CV curves at scan rates of 20, 40, 60, 80, and 100 mV s^{-1} and found in the order of NZN400 > NZN200 > NZN600, which is 10.00 cm^2 for NZN400, 2.11 cm^2 for NZN200, and 1.36 cm^2 for NZN600. ECSA normalized LSV profiles of NZN200, NZN400, and NZN600 can be found in Fig. S15. Fig. S7(b–d) shows the CV curves of all nanostructures in non-faradaic regions.

Fig. 4f depicts the Electrochemical Impedance Spectroscopy (EIS) spectra for NZN200, NZN400, and NZN600. EIS is a highly effective technique for gaining useful insights into an electrocatalyst's charge transfer resistance and ion/electron transport characteristics.[55] The equivalent fitted circuit is shown in SI Fig. S8. The R_s value, which is the resistance given by the electrolyte and electrical contacts, is the lowest for NZN400, at 1.23 Ω, followed by NZN200 at 2.84 Ω and NZN600 at 3.179 Ω. In addition, the R_{ct} value is utilized to determine charge transfer at the electrode–electrolyte interface. For NZN400, the R_{ct} is 1.45 Ω, in contrast to NZN200 and NZN600, which showed R_{ct} values of 2.12 Ω and 6.36 Ω, respectively, indicating improved charge transfer kinetics and thus superior OER kinetics. Thus, EIS reveals that NZN400 exhibits quick charge transfer and low resistance, making it an effective OER catalyst. Furthermore, symmetric device testing is performed to create a baseline assessment of the electrochemical behaviour under ideal conditions, employing NZN400 electrodes at both the anode and cathode (Fig. 4g). The LSV curve demonstrated an overpotential value of 750 mV in 1 M KOH at a current density of 20 mA cm^{-2} and a scan rate of 2 mV s^{-1}. Also, this testing showed that the catalyst requires a cell voltage of 1.85 V at 10 mA cm^{-2}. To assess the long-term durability of the optimized NZN400 electrode, a chronopotentiometry test was performed for 22 hours at a constant current density of 10 mA cm^{-2}, as shown in Fig. 4h. The voltage retention for this sample was found to be 99.80%, showing good stability over long test periods. Notably, the turnover frequency (TOF) is calculated using an additional SI eqn (4). NZN400 showed the highest TOF value of 0.018 s^{-1} as compared to NZN200 and NZN600, which showed TOF values of 0.012 s^{-1} and 0.005 s^{-1}, respectively. Fig. 4i shows the TOF *vs.* overpotential variation. Furthermore, to investigate the catalytic effectiveness of the catalyst material per unit mass, mass activity was calculated using SI eqn (5). NZN400 showed the highest mass activity of 16.27 A g^{-1} among others, demonstrating superior OER performance. Consistently, the optimized sample NZN400 had significantly higher mass activity values, which were consistent with earlier electrochemical tests. Fig. S7(e) shows the iR drop for all samples estimated using (Galvanostatic Charge Discharge) GCD, which reflects the voltage drop across the electrolyte. Notably, NZN400 showed the lowest slope, indicating negligible voltage loss during the OER process. Table 1 lists all the parameter values. Fig. S16(a)–(i) shows the electrocatalytic performance parameter testing of NZN nanostructures in the Hg/HgO reference electrode configuration. These findings demonstrate NZN400's stability and efficiency, indicating its potential as a viable catalyst for electrochemical applications.

3.7 Electrochemical half-cell supercapacitor performance

The electrochemical half-cell energy storage characteristics of the synthesized $NiO/Zn_3N_2/C_3N_4$ (NZN) nanostructure were evaluated using a three-electrode setup. The self-supported NZN (200, 400, and 600) heterointerfaces served as the working electrode, Ag/AgCl as the reference electrode, and a platinum (Pt) electrode as the counter electrode. All measurements were performed in 1 M Na_2SO_4 electrolyte. Electrochemical performance was evaluated using techniques like CV, GCD, and EIS. Fig. 5a shows the CV profile comparison at 10 mV s^{-1} of NZN200, NZN400, and NZN600. NZN400 exhibited the highest enclosed area under the CV curve, depicting the maximum specific capacitance. Also, CV curves demonstrated significant redox peaks for NZN400, implying a pseudocapacitive nature due to faradaic redox reactions ($Ni^{2+} \leftrightarrow Ni^{3+} + e^-$). In contrast, NZN200 showed less intense redox peaks, possibly due to inadequate phase formation or insufficient crystallization, resulting in reduced electrochemical performance. On the other hand, NZN600 exhibits suppressed peaks, which might be due to excessive grain growth or a wrinkled agglomerated structure, leading to reduced active sites at high temperature.

NZN400 shows the highest enclosed area in the CV profile with prominent redox peaks suggesting a strong pseudocapacitive behaviour, which results from the Ni^{2+}/Ni^{3+} redox transformations. The close synergetic effects of NiO, Zn_3N_2, and g-C_3N_4 result in efficient ion/electron transport, which results in effective faradaic reactions, leading to the highest specific capacitance. NZN200, on the other hand, has decreased crystallinity and inadequate phase formation in comparison, and shows weak redox peaks and reduced enclosed area in CV, depicting a combination of electric double layer capacitance and pseudo capacitance. The decreased active sites and lower

Table 1 List of values of the electrochemical OER performance parameters for NZN200, 400, and 600

S. no.	Sample name	Overpotential (η_{50}) (mV)	Tafel slope (mV dec^{-1})	ECSA (cm^2)	Mass activity (A g^{-1})	TOF (s^{-1})
1	NZN200	470	175	2.11	11.71	0.012
2	NZN400	350	85	10.00	16.27	0.018
3	NZN600	600	376	1.36	5.09	0.005

conductivity result in decreased specific capacitance. NZN600, at last, which is annealed at very high temperatures, exhibits a repressed CV curve and diminished redox activity. Deformation of g-C_3N_4 and nitrogen loss from Zn_3N_2 leads to a decreased number of active sites and conductivity. Furthermore, the distorted morphology will lead to decreased ion transport and decreased specific capacitance. The observations indicate that the different capacitive behaviour depends on proper phase formation, interface quality, and defect density. SI Fig. S9a and b display additional CV curves of NZN200 and NZN600 at scan rates ranging from 10 mV s^{-1} to 100 mV s^{-1}. Fig. 5c shows the GCD profiles of composite structures. NZN400 exhibits the longest charge–discharge duration, which confirms its highest capacitance. The observation of a minor voltage plateau, which aligns well with the nature of CV curves and well in line with CV analysis, further supports the pseudocapacitive behaviour associated with faradaic reactions.[56] The nearly symmetric charge–discharge curves, which also suggest a strong coulombic efficiency, are indicative of excellent electrochemical reversibility. Fig. S9c shows the specific capacitance comparison of NZN200, NZN400, and NZN600 with scan rates. The GCD profiles for NZN200 and NZN600 are illustrated in SI Fig. S9d & e and were acquired at current densities ranging from 2 to 7 mA cm^{-2}. Fig. 5e illustrates the rate capacity of these nanostructure electrodes by illustrating the change in specific capacitance as a function of varied current densities. NZN400 showed a specific capacitance value of 124 mF cm^{-2} at 2 mA cm^{-2}, which was found to be higher than that of NZN200 and NZN600, which exhibited a capacitance value of 39.6 mF cm^{-2} and 15.4 mF cm^{-2} at similar current densities. Fig. 5b shows the CV cycles of the NZN400 nanostructure, which demonstrate capacitive behaviour as the scan rate increases. The area under the CV curve increases with scan rate due to effective interaction of the electrolyte ions with the electrode materials.[57] Fig. 5d shows the GCD profiles of NZN00 at different current densities. To conduct a more thorough estimation of the electrochemical performance, EIS measurements were carried out (Fig. 5f). The Nyquist plot demonstrates that NZN400 exhibits the minimum charge transfer resistance (R_{ct}) of 19.7 Ω, suggesting enhanced kinetics for electron and ion transport. In addition, NZN400 demonstrated outstanding electrolyte accessibility and solution kinetics, with a solution resistance (R_s) of 3.42 Ω. The electrochemical parameters for each heterointerface are presented in Table 2. The findings suggest that NZN400 is a promising electrode material for high-performance supercapacitors, attributed to its exceptional electrochemical stability, remarkable rate capability, and improved specific capacitance.

Table 2 List of values of the electrochemical supercapacitance performance parameters for NZN200, 400, and 600

S. no.	Sample	Specific capacitance (mF cm^{-2})	R_{ct} (Ω)	R_s (Ω)
1	NZN200	39.6	675	5.10
2	NZN400	124	19.7	3.42
3	NZN600	15.4	681	5.50

3.8 Coin cell supercapacitor performance

The electrochemical performance of the NiO/Zn_3N_2/graphitic carbon nitride coin cell supercapacitor was examined employing various electrochemical approaches. Fig. 6a illustrates the

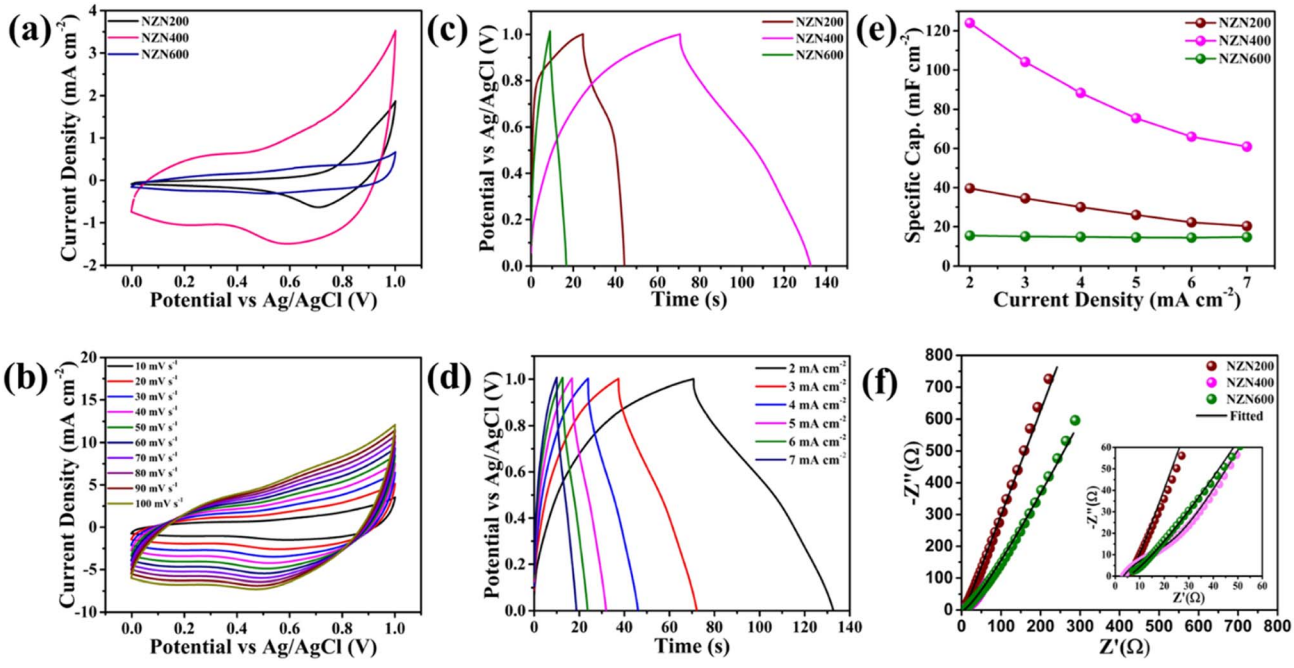

Fig. 5 Half-cell supercapacitance performance, (a) comparative CV profiles of NZN200, NZN400 and NZN600, (b) CV profiles of NZN400 at different scan rates, (c) GCD profiles of NZN200, NZN400 and NZN600, (d) GCD profiles of NZN400 at different current densities, (e) specific capacitance *vs.* current density of heterointerfaces and (f) EIS spectra of all nanostructures.

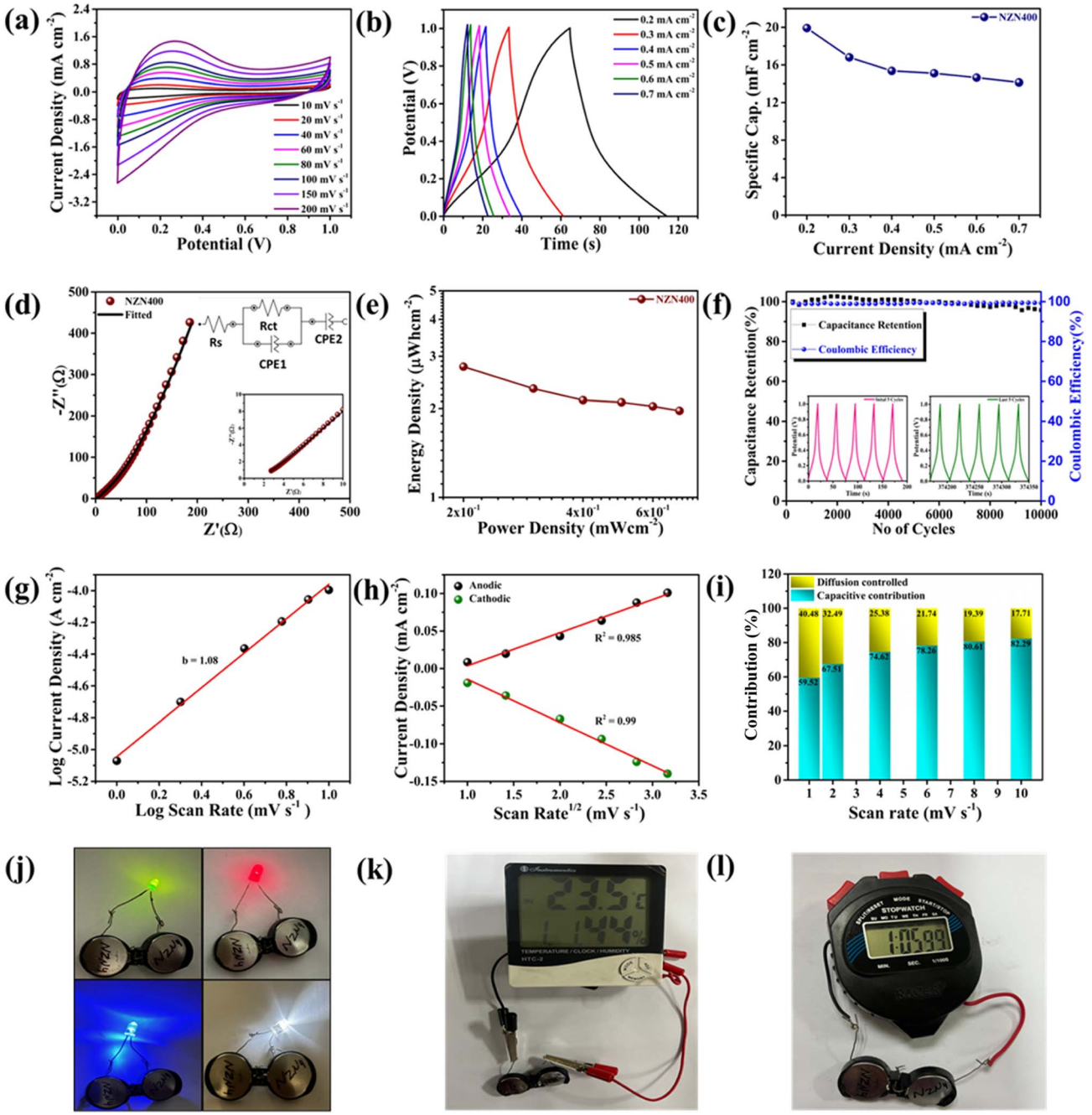

Fig. 6 (a) CV cycles of the NZN400 coin cell device, (b) GCD profiles of the NZN400 device, (c) specific capacitance *vs.* current density, (d) EIS spectrum of NZN400, (e) Ragone plot, (f) stability and coulombic efficiency plot, (g) *b* value calculation, (h) plots of anodic and cathodic peak current density *vs.* scan rate$^{1/2}$, (i) capacitive and diffusion contribution of the NZN400 device and (j)–(l) powering commercial LEDs, a digital hygrometer and a digital stopwatch, respectively.

cyclic voltammetry (CV) cycles of NZN400 at various scan rates. The CV curves exhibit distinct redox peaks, signifying pseudocapacitive behaviour resulting from faradaic redox transitions of Ni^{2+}/Ni^{3+}. Fig. 6b shows the GCD profiles of NZN400 at different current densities. The nonlinear charge–discharge nature of the curves may account for the pseudocapacitive behaviour of the nanostructure. Fig. 6c shows the specific capacitance *vs.* scan rate of NZN400. It showed the highest specific capacitance value of 19.92 mF cm^{-2} at 0.2 mA cm^{-2}. Fig. 6d illustrates the Nyquist plot of the NZN400 device, displaying a slight semicircle in the high-frequency domain, with a low charge transfer resistance (R_{ct}) of 175 Ω, which, as compared to the half-cell, is high due to the use of a separator that causes kinetic constraints. In the low-frequency regime, a sharp curve signifies the optimum capacitive performance. The inset of Fig. 6d shows the equivalent fitted circuit comprised of solution resistance with a value of 1.75 Ω, and charge transfer resistance (R_{ct}) with two constant phase

elements (CPE_1 and CPE_2). Fig. S10 also shows the equivalent circuit modelling, besides EIS performance parameters for both half-cell and coin cell supercapacitor devices.

Fig. 6e shows the Ragone plot, which represents the relationship between energy density and power density. The NZN400 device showed an energy density of 2.7 μW h cm^{-2} at 0.2 mA cm^{-2} and a power density of 0.2 mW cm^{-2} at 0.2 mA cm^{-2}. This trend of decrease in energy density with increasing power density highlights the trade-off between rapid charge–discharge capability and total charge storage. Fig. 6f demonstrates the cycling stability and coulombic efficiency of the NZN400 device. Excellent stability over 10 000 cycles with a retention rate of 95.7% reveals the durability and robustness of the fabricated device. Additionally, the coulombic efficiency of 99.4% suggests high reversibility of charge storage mechanisms with bare or no material degradation.

The quantitative diffusion properties of the NZN400 device are examined using Dunn's method. This method indicates the difference between surface capacitive and diffusion-controlled contributions at different scan rates at the applied potential. At a constant potential, a changing current can be represented by using the equation[58]

$$I(V) = K_1(v) + K_2(v)^{1/2} \quad (1)$$

where K_1 is the capacitive factor and K_2 represents the diffusion-controlled factor, with v indicating the scanning rate in mV s^{-1}. Additionally, the b value can be determined using the power law from the relationship between the peak current (I) and scan rate (v).[58]

$$I = av^b \quad (2)$$

The determination of the diffusion-controlled contribution and the capacitive contribution depends on the value of b. When the CV shape is rectangular and the value of b equals 1, the electrode material demonstrates EDLC behaviour.[59] When the CV shape resembles a rectangle with several points of inflection and the value of b is close to 0.5, the material demonstrates pseudocapacitive behaviour due to fast redox reactions.[59] The NZN400 device showed a slope b = 1.08 (Fig. 6g). Fig. 6i shows the capacitive and diffusion-controlled contribution of the NZN400 device with scan rate. At lower scan rates (1–3 mV s^{-1}), the contribution from diffusion control is more significant (*i.e.* 32.49% at 2 mV s^{-1}). The increase in scan rate leads to a systematic increase in the capacitive contribution, from 59.52% at 1 mV s^{-1} to 78.26% at 6 mV s^{-1}. At higher scan rates (7–10 mV s^{-1}), the capacitive behaviour dominates, reaching 82.29% at 10 mV s^{-1}. Fig. S11(a) shows the specific capacitance variation of the NZN400 device with scan rate, and Fig. S11(b) shows the CV curves of the same recorded at low scan rates.

Furthermore, a fabricated coin cell supercapacitor was tested for real-time applications (Fig. 6j–l), including charging of different commercial LEDs, a digital hygrometer for 5 minutes, and a digital stopwatch over 50 minutes (SI Videos 1 & 2). The robust performance of NZN400 in real-time operations underscores its promise for futuristic energy storage technologies. Table S3 shows the comparison of the electrochemical energy density of the present work with similar materials.

Apart from the above-mentioned claims and experiments, the exceptional energy conversion and storage capabilities of NZN400 are mostly due to the following material characteristics.

- Using a balanced mechanism of EDLC and faradaic reactions, the integration of NiO, Zn_3N_2, and g-C_3N_4 enhances charge storage.
- Employing nickel foam as a substrate improves interfacial contact with active materials, hence reducing interfacial resistance and enhancing charge transfer kinetics.[60]
- The coexistence of mixed oxidation states (Ni^{2+}/Ni^{3+} and Zn^{2+}) alongside surface oxygen species augments electronic conductivity and charge redistribution, leading to a notable enhancement in energy storage and OER kinetics.

4. Electrochemical kinetics, *ex situ* and *in situ* analysis

A higher rate constant value substantially influences the catalytic efficiency and overall performance by facilitating rapid electron or ion movement. Fig. 7a–c shows the anodic and cathodic peak current *vs.* the square root of the scan rate of NZN heterostructures.

The rate constant k_0 and transfer coefficient α can be calculated using the Nicolson dimensional number and Laviron equation[61,62] respectively using the following equations:

$$\Psi = k_0\left(\frac{D_0}{D_R}\right)^{\alpha/2}\sqrt{\frac{RT}{\pi nFD_0\vartheta}} \quad (3)$$

$$\alpha = \frac{\delta_{pa}}{\delta_{pa} + \delta_{pc}} \quad (4)$$

In eqn (3), D_0 and D_R are the diffusion coefficients during the oxidation and reduction process, respectively, R is the universal gas constant, T is the temperature in Kelvin, and F is the Faraday constant.

In eqn (4), δ_{pa} and δ_{pc} are the slopes calculated from currents recorded from anodic and cathodic peaks *vs.* the logarithm of scan rate plots, respectively.

If we consider $D_0 \cong D_R$, then eqn (3) can be rewritten as:

$$\Psi \cong k_0\sqrt{\frac{RT}{\pi nFD_0\vartheta}} \quad (5)$$

Additionally, Ψ can be calculated as:

$$\Psi = \frac{-0.6288 + 0.0021\Delta E_P}{1 - 0.017\Delta E_P} \quad (6)$$

Utilizing eqn (5) and (6), the value of k_0 can be calculated as the slope of Ψ *versus* $v^{-1/2}$.

Fig. 7d–f shows the anodic and cathodic peak current slopes against the log of scan rates of NZN200, NZN400, and NZN600, respectively. The corresponding Ψ and rate constant variations

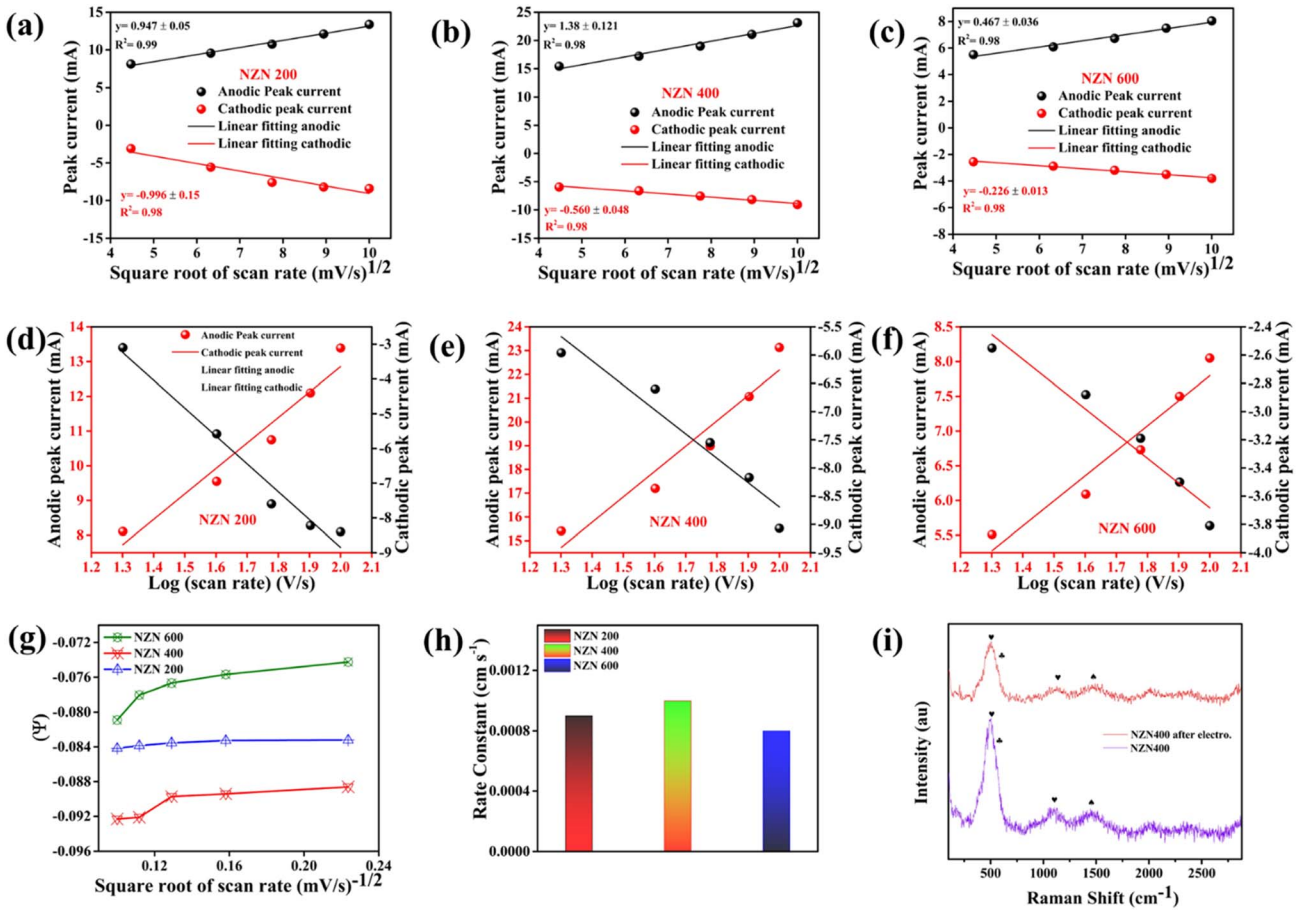

Fig. 7 (a)–(c) The anodic and cathodic peak current *vs.* the square root of the scan rate of NZN heterostructures. (d–f) The anodic and cathodic peak current slopes against the log of scan rates of NZN200, NZN400, and NZN600, respectively. (g) Ψ estimation and (h) rate constant variation. (i) Postmortem Raman spectra of NZN400 before and after the electrochemical stability test.

are shown in Fig. 7g and h, respectively. NZN400 shows a rate constant value of 0.001 s^{-1}, which is higher as compared to that of NZN200 and NZN600, which show a value of 0.009 s^{-1} and 0.0008 s^{-1}, suggesting faster kinetics in NZN400. Fig. S18 presents the CV of NZN200, NZN400, and NZN600 in the redox active electrolyte. Fig. 7i shows the post-mortem Raman spectra of NZN400, showing no change and robustness of the electrocatalyst synthesized. Fig. S17 shows the fitted C_{dl} slope of NZN nanostructures in the Ag/AgCl reference electrode. Fig. S18 shows CV of NZN200, NZN400, and NZN600 in redox active electrolyte.

4.1 Post-mortem and *ex situ* characterization studies

Fig. S14 shows the postmortem FESEM and EDS of the NZN400 nanostructure after the electrochemical stability test, revealing the robust nature that maintains the structural and elemental integrity with little agglomeration due to K ions. Fig. 8b shows the deconvoluted Ni 2p XPS spectrum for NZN400 before and after the stability test. A small shift in Ni 2p B.E. values towards higher B.E. after stability can be attributed to oxidation of Ni^{2+}/Ni^{3+}. Fig. 8c shows the deconvoluted Zn 2p spectra with minimal change in the B.E., depicting the robustness of zinc metal. Fig. 8d shows a comparison of C 1s spectra, which shows an additional peak at 289.5 eV for NZN400 after electrochemical measurements which can be assigned to the C=O bond (oxidation) due to prolonged cycles. In the O 1s spectra (Fig. 8e), the reduced intensity of the Ni^{2+} signal can be attributed to the partial oxidation of Ni^{2+} species in NiO to Ni^{3+}/Ni^{4+}, resulting in the formation of highly active NiOOH-like intermediates. Fig. 8f shows the minimal shift in the C–N–H bond, which corresponds to the stretching due to long-term cycling tests. Fig. 8g shows the XRD spectrum before and after electrochemical stability testing, showing no change or any additional peaks, further confirming the robustness of the nanostructures. Fig. S19–S21 shows the effect of nitrogen environment on the adsorption of OH^- ions *via* wetting, double layer capacitance calculation and LSV profiles, showing that the nitrogen environment can effectively alter the overall electrochemical performance. Fig. S24 shows EIS, *I–V* and sheet resistance of NZN400 and without g-C_3N_4. Fig. S26 presents the JCPDS file no assigned to NZN heterostructures.

4.2 Reaction order analysis

We have measured the LSV profiles of NZN400 at different electrolyte concentrations (0.1 M, 0.2 M, 0.3 M, 0.4 M, 0.6 M, 1 M, 2 M and 4 M) and plotted the log (current density) *vs.* log

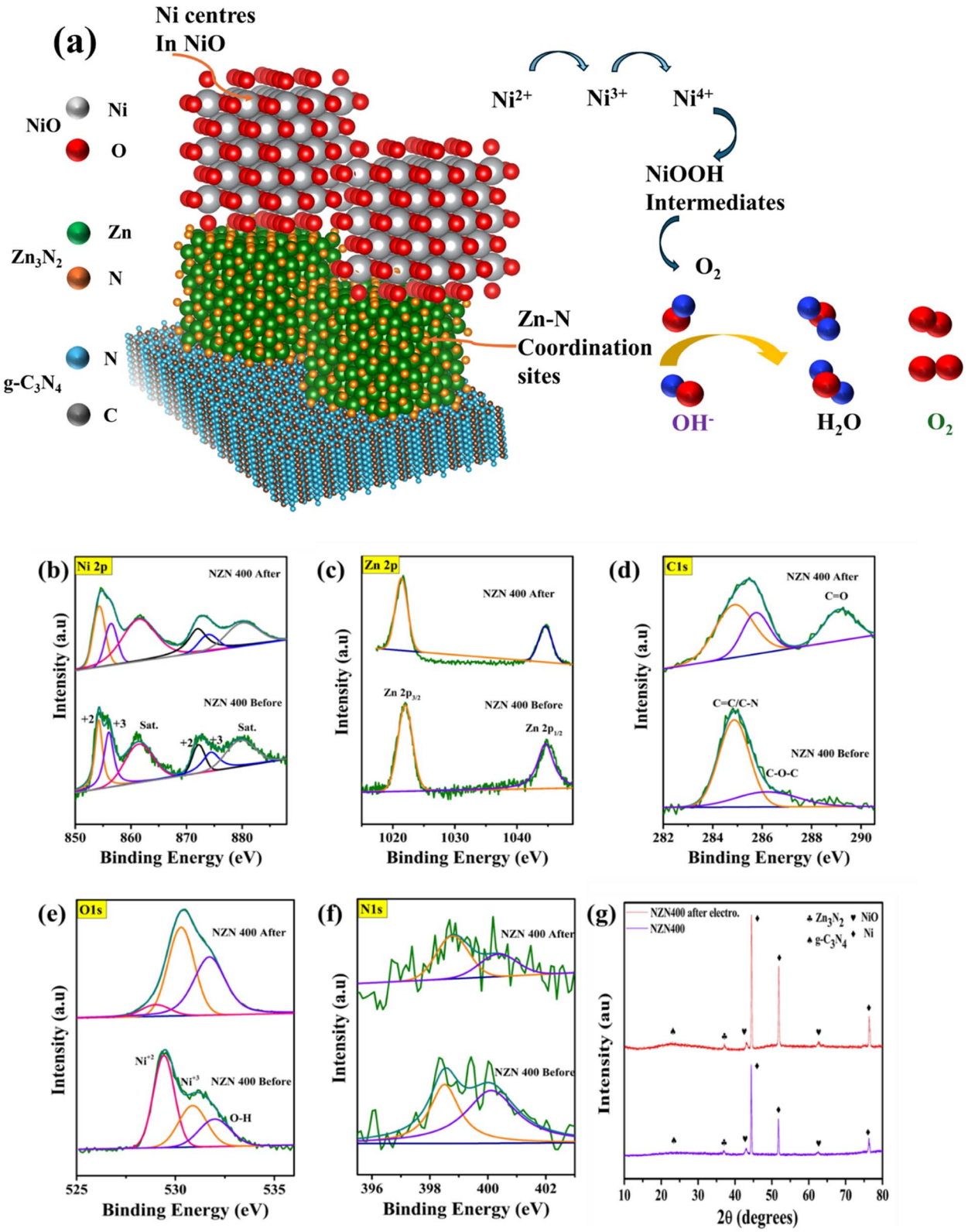

Fig. 8 (a) Mechanistic visualization of OER activity, postmortem XPS spectra of NZN400: (b) Ni 2p, (c) Zn 2p, (d) C 1s, (e) O 1s, and (f) N 1s, and (g) postmortem XRD of NZN400.

(OH^-) to get the corresponding slope (Fig. S22). The value of the slope generally indicates the reaction order. The obtained slope 1.02 provides the reaction order corresponding to hydroxide ions. It means $j \propto [OH^-]^{1.02}$ or first order dependence on OH^- in the tested range. This value indicates the involvement of one OH^- as a reactant in the elementary rate determining state. In

alkaline media, this suggests OH adsorption ($* + OH^- \rightarrow *OH + e^-$) or the deprotonation/dehydroxylation of an adsorbed hydroxyl ($*OH + OH^- \rightarrow *O + H_2O + e^-$).

4.3 Kinetic isotope effect

To further analyse the information about the intermediate's behaviours, we calculated the kinetic isotope effect parameter KIE *via* testing of NZN400 in 1 M KOH and 1 M D_2O solutions (Fig. S23). KIE $= K_H/K_D$ with a value of 3.4 in a different overpotential range indicates proton involvement implying OH bond stretching and contributing directly to the rate determining step. The semiclassical approximation of this value leads to a zero-point energy difference $\Delta ZPE = RT \ln 3.4 \cong 3.0$ kJ mol^{-1}. This KIE values outclass the RDS agreements of purely electron transfer limited step or entirely chemical O–O coupling which exhibits typically a KIE value of 1.

4.4 *In situ* EIS analysis

In situ EIS was recorded after every 5 GCD cycles at 4 mA cm^{-2} to understand the Na^+ transport behaviour under operating conditions (Fig. S25). The Nyquist spectra at 0, 5, 10, 15, 20, 25 and 30 cycles show almost no major change. A slight increase in resistance is observed after the initial 5 cycles compared to the fresh cell which may be due to initial wetting/activation of the electrode–electrolyte interface. After that, the spectra remain stable with very small variations.[63,64] The high-frequency intercept (R_s) remained constant which suggests stable Na^+ conduction in the electrolyte and at the electrode/electrolyte interface. The semicircle diameter (R_{ct}) also did not change much, indicating fast and reversible adsorption desorption of Na^+ ions at the redox active sites. The low frequency region line remains nearly vertical which shows that Na^+ diffusion in porous electrode channels and capacitive charge storage was maintained even after several cycles. These results clearly prove that the NZN400 electrode provides stable Na^+ ion transport pathways and supports the excellent cycling stability of the device.

5. Conclusion

In summary, we have integrated transition metal heteroatoms to fabricate a hybrid nanostructure, which is further utilised for bifunctional applications in energy conversion and storage. Synergetic interactions between such heterointerfaces facilitate the charge transfer characteristics and increase the active sites. The optimized catalyst NZN400 demonstrated excellent OER activity with a low overpotential of 350 mV in addition to remarkable coin cell device performance, which exhibited a specific capacitance value of 19.92 mF cm^{-2} and excellent stability with real-time applications. The presence of mixed oxidation states (Ni^{2+}/Ni^{3+}, Zn^{2+}) in conjunction with surface oxygen species enhances electronic conductivity and charge redistribution, resulting in a significant improvement in energy storage and OER kinetics. These hybrid nanostructures offer significant insights for the advancement of efficient, durable, and affordable catalysts designed for commercial storage and electrolysis technology.

Author contributions

Tanuja Singh: conceptualization, methodology, formal analysis, data curation, writing – original draft, writing – review & editing, validation. Deepak Deepak: conceptualization, methodology, investigation, validation. Abhishek Panghal: methodology, investigation, software, visualization. Shailendra Kumar Saxena: investigation, data curation, formal analysis. Barnali Mahato: investigation, visualization, formal analysis. Abhishek S Shekhawat: investigation, data curation. Susanta Sinha Roy: conceptualization, investigation, formal analysis, data curation, supervision, validation, visualization, writing – review & editing.

Conflicts of interest

The authors declare that they have no known competing financial interests or personal relationships that could have appeared to influence the work reported in this paper.

Data availability

The results of this research are corroborated by the data which can be obtained from the corresponding author upon request. The data which support these findings can be found in the paper.

Supplementary information: FESEM images, EDS mapping, HRTEM images, XPS spectra, CV curves at different scan rates, LSV curves, GCD, equivalent circuit modelling, electrochemical performance parameters in Hg/HgO, postmortem studies, reaction order, *etc.* Fig. S1–S26. See DOI: **https://doi.org/10.1039/d5ta05959c**.

Acknowledgements

Tanuja Singh acknowledges the financial support from the Shiv Nadar Institution of Eminence (SNIoE), India, through a scholarship. Authors acknowledge the Nanotechnology Research Centre (NRC) SRMIST, KTR, for providing the facilities for XPS measurements. We also acknowledge support from the FIST Project (Sanction Number SR/FST/PS-I/2017/6(C)) for the Raman measurements.

References

1 Z. Sun, L. Sun, S. W. Koh, J. Ge, J. Fei, M. Yao, W. Hong, S. Liu, Y. Yamauchi and H. Li, *Carbon Energy*, 2022, **4**, 1262–1273.
2 G. M. Tomboc, J. Kim, Y. Wang, Y. Son, J. Li, J. Y. Kim and K. Lee, *J. Mater. Chem. A*, 2021, **9**, 4528–4557.
3 H. Tüysüz, *Acc. Chem. Res.*, 2024, **57**, 558–567.
4 A. G. Olabi, Q. Abbas, A. Al Makky and M. A. Abdelkareem, *Energy*, 2022, **248**, 123617.
5 T. Singh, D. Deepak, A. Panghal and S. S. Roy, *Int. J. Hydrogen Energy*, 2024, **84**, 939–950.

6 S. Mohanapriya, P. Dhanasekaran and S. V. Selvaganesh, Noble Metal-Free Electrocatalysts: Fundamentals and Recent Advances in Electrocatalysts for Energy Applications, *Am. Chem. Soc.*, 2022, **1431**, 4–73.
7 A. Udayakumar, P. Dhandapani, S. Ramasamy, C. Yan and S. Angaiah, *Ionics*, 2024, **30**, 61–84.
8 D. Deepak, T. Singh, A. Mahapatra, A. Panghal, C. Nagesh and S. S. Roy, *Adv. Sustain. Syst.*, 2025, **9**, 2400656.
9 M. Sohail, S. Rauf, M. Irfan, A. Hayat, M. M. Alghamdi, A. A. El-Zahhar, D. Ghernaout, Y. Al-Hadeethi and W. Lv, *Nanoscale Adv.*, 2024, **6**, 1286–1330.
10 G. G. Njema and J. K. Kibet, *Prog. Eng. Sci.*, 2024, 100018.
11 F. Wang, X. Wu, X. Yuan, Z. Liu, Y. Zhang, L. Fu, Y. Zhu, Q. Zhou, Y. Wu and W. Huang, *Chem. Soc. Rev.*, 2017, **46**, 6816–6854.
12 M. Hepel, *Electrochem. Sci. Adv.*, 2023, **3**, e2100222.
13 S. V Prabhakar Vattikuti, K. C. Devarayapalli, M. Chandra Sekhar, N. Kumar Reddy Nallabala, N. Nguyen Dang and J. Shim, *Mater. Lett.*, 2021, **285**, 129203.
14 B. Tang, Y. Wei, R. Jia, F. Zhang and Y. Tang, *Small*, 2024, **20**, 2308126.
15 A. Panghal, T. Singh, D. Deepak, R. Kumar and S. S. Roy, *J. Energy Storage*, 2025, **115**, 115981.
16 A. Panghal, D. Sahoo, D. Deepak, S. Deshmukh, B. Kaviraj and S. S. Roy, *ACS Appl. Nano Mater.*, 2024, **7**, 5358–5371.
17 J. Rehman, K. Eid, R. Ali, X. Fan, G. Murtaza, M. Faizan, A. Laref, W. Zheng and R. S. Varma, *ACS Appl. Energy Mater.*, 2022, **5**, 6481–6498.
18 B. Gao, X. Li, K. Ding, C. Huang, Q. Li, P. K. Chu and K. Huo, *J. Mater. Chem. A*, 2019, **7**, 14–37.
19 D. Deepak, J. Raghav, A. Panghal, T. Singh, S. Roy and S. S. Roy, *J. Alloys Compd.*, 2024, **978**, 173391.
20 R. Paulose, R. Mohan and V. Parihar, *Nano-Struct. Nano-Objects*, 2017, **11**, 102–111.
21 D. Wang, C. Zhang, J. Hu, T. Zhuang and Z. Lv, *J. Colloid Interface Sci.*, 2024, **655**, 217–225.
22 A. Nashim, S. Pany and K. Parida, *RSC Adv.*, 2024, **14**, 233–244.
23 Y.-Y. Xie, H.-J. Chen, Q.-Y. Bai, X.-L. Wang, G. Wu, S.-C. Chen and Y.-Z. Wang, *Electrochim. Acta*, 2021, **390**, 138772.
24 J. Nama and S. Sharma, *ACS Appl. Energy Mater.*, 2024, **7**, 10407–10416.
25 H. M. Tofail, R. Ghazi, F. A. Ghaeb, R. N. Dara, I. Kebaili, I. Boukhris, H. Ding and Z. U. Rehman, *Sustainable Energy Fuels*, 2025, **9**, 2900–2927.
26 K. Bhunia, S. Khilari, M. Chandra, D. Pradhan and S.-J. Kim, *J. Alloys Compd.*, 2023, **935**, 167842.
27 Y. Li, V. Verma, H. Su, X. Zhang, S. Zhou, T. Lawson, J. Li, R. Amal, Y. Hou and L. Dai, *Adv. Energy Mater.*, 2024, **14**, 2401341.
28 N. AbouSeada, M. G. Elmahgary, S. O. Abdellatif and K. Kirah, *J. Alloys Compd.*, 2024, **1002**, 175325.
29 A. A. Ensafi, M. M. Abarghoui and B. Rezaei, *Ceram. Int.*, 2019, **45**, 8518–8524.
30 D. Laniel, A. A. Aslandukova, A. N. Aslandukov, T. Fedotenko, S. Chariton, K. Glazyrin, V. B. Prakapenka, L. S. Dubrovinsky and N. Dubrovinskaia, *Inorg. Chem.*, 2021, **60**, 14594–14601.
31 R. Adalati, A. Kumar, M. Sharma, P. Tiwari and R. Chandra, *Appl. Phys. Lett.*, 2020, **117**, 123904.
32 H. Yang, H. Guo, K. Pang, P. Fan, X. Li, W. Ren and R. Song, *Nanoscale*, 2020, **12**, 7024–7034.
33 R. Naik, H. P. Nagaswarupa, B. H. M. Darukesha and D. M. Tejashwini, *Advances in Space Radiation Detection: Novel Nanomaterials and Techniques*, Springer Nature Switzerland, Cham, 2024, pp. 23–36.
34 N. Srinivasa, J. P. Hughes, P. S. Adarakatti, C. Manjunatha, S. J. Rowley-Neale, S. Ashoka and C. E. Banks, *RSC Adv.*, 2021, **11**, 14654–14664.
35 M. R. Islam, A. K. Chakraborty, M. A. Gafur, M. A. Rahman and M. H. Rahman, *Res. Chem. Intermed.*, 2019, **45**, 1753–1773.
36 A. Trapalis, J. Heffernan, I. Farrer, J. Sharman and A. Kean, *J. Appl. Phys.*, 2016, **120**, 205102.
37 P. Kathiravan, K. Thillaivelavan, G. Viruthagiri and N. Shanmugam, *J. Indian Chem. Soc.*, 2024, **101**, 101171.
38 E. Scattolin, M. Benedet, G. A. Rizzi, A. Gasparotto, O. I. Lebedev, D. Barreca and C. Maccato, *ChemSusChem*, 2024, **17**, e202400948.
39 W. Huang, S. Ding, Y. Chen, W. Hao, X. Lai, J. Peng, J. Tu, Y. Cao and X. Li, *Sci. Rep.*, 2017, **7**, 5220.
40 Y. S. Chen, J. F. Kang, B. Chen, B. Gao, L. F. Liu, X. Y. Liu, Y. Y. Wang, L. Wu, H. Y. Yu, J. Y. Wang, Q. Chen and E. G. Wang, *J. Phys. D Appl. Phys.*, 2012, **45**, 65303.
41 D. S. Mann, S.-N. Kwon, S. Thakur, P. Patil, K.-U. Jeong and S.-I. Na, *Small*, 2024, **20**, 2311362.
42 H. Wang, X. Li, Q. Ruan and J. Tang, *Nanoscale*, 2020, **12**, 12329–12335.
43 M. Ge, X. Li, M. Zhang and Z. Liu, *J. Inorg. Organomet. Polym. Mater.*, 2022, **32**, 678–686.
44 A. Dogra, A. Kumar, M. Kapoor and N. Gupta, *ChemistrySelect*, 2021, **6**, 7118–7122.
45 S. Yadav, A. Singh and A. K. Choubey, *J. Alloys Compd.*, 2024, **979**, 173422.
46 P.-C. Wei, S.-C. Tong, C.-M. Tseng, C.-C. Chang, C.-H. Hsu and J.-L. Shen, *J. Appl. Phys.*, 2014, **116**, 143507.
47 A. Mahapatra, R. S. Ajimsha, D. Deepak and P. Misra, *Sci. Rep.*, 2024, **14**, 11871.
48 A. J. Addie, M. A. Mohammed and R. A. Ismail, *Mater. Sci. Semicond. Process.*, 2022, **145**, 106664.
49 H. Wang, X. Zhang, J. Xie, J. Zhang, P. Ma, B. Pan and Y. Xie, *Nanoscale*, 2015, **7**, 5152–5156.
50 Q. Xiang, J. Yu and M. Jaroniec, *J. Phys. Chem. C*, 2011, **115**, 7355–7363.
51 N. Zhang, Y. Hu, L. An, Q. Li, J. Yin, J. Li, R. Yang, M. Lu, S. Zhang and P. Xi, *Angew. Chem.*, 2022, **134**, e202207217.
52 A. Haruna, K. B. Dönmez, S. Hooshmand, E. Avcı, M. Qamar, S. A. Zaidi, F. Shahzad, T. S. Miller, B. K. Chakrabarti, C. A. Howard and M. K. Bayazıt, *Carbon*, 2024, **226**, 119177.
53 X. Zhang, L. Zhang, Y. Zhu, Z. Li, Y. Wang, T. Wågberg and G. Hu, *ChemSusChem*, 2021, **14**, 467–478.
54 D. Antipin and M. Risch, *Electrochem. Sci. Adv.*, 2023, **3**, e2100213.

55 M. Y. Perdana, B. A. Johan, M. Abdallah, M. E. Hossain, M. A. Aziz, T. N. Baroud and Q. A. Drmosh, *Chem. Rec.*, 2024, **24**, e202400007.
56 Y. Li, T. Liu, Y. Liu, F. Meng and Z. Cao, *Chem. Eng. J.*, 2024, **479**, 147906.
57 T. Kedara Shivasharma, A. C. Mendhe, R. Sahu and B. R. Sankapal, *J. Colloid Interface Sci.*, 2024, **676**, 739–754.
58 D. B. Bailmare, P. Tripathi, A. D. Deshmukh and B. K. Gupta, *Sci. Rep.*, 2022, **12**, 3084.
59 S. Sharma and P. Chand, *Results Chem.*, 2023, **5**, 100885.
60 L. Lyu, J. Kang, K. Seong, C. W. Kim, J. Lim and Y. Piao, *J. Alloys Compd.*, 2021, **872**, 159610.
61 M. C. C. G. Carneiro, F. T. C. Moreira, R. A. F. Dutra, R. Fernandes and M. G. F. Sales, *Microchem. J.*, 2018, **138**, 35–44.
62 I. Lavagnini, R. Antiochia and F. Magno, *Electroanalysis*, 2004, **16**, 505–506.
63 P. Xu, M. Xu, J. Zhang, J. Zou, Y. Shi, D. Luo, D. Wang, H. Dou and Z. Chen, *Angew. Chem., Int. Ed.*, 2024, **63**, e202407909.
64 Y. Shao, W. Lu, T. Zhang, B. Yin, B.-B. Xie, J. Ning and Y. Hu, *Carbon Energy*, 2025, **7**, e701.